PAPER

Measurement and mitigation of free convection in microfluidic gradient generators†

Yang Gu, Varun Hegde and Kyle J. M. Bishop [iD] *

Microfluidic gradient generators are used to study the movement of living cells, lipid vesicles, and colloidal particles in response to spatial variations in their local chemical environment. Such gradient driven motions are often slow (less than 1 μm s^{-1}) and therefore influenced or disrupted by fluid flows accompanying the formation and maintenance of the applied gradient. Even when external flows are carefully eliminated, the solute gradient itself can drive fluid motions due to combinations of gravitational body forces and diffusioosmotic surface forces. Here, we develop a microfluid gradient generator based on the *in situ* formation of biopolymer membranes and quantify the fluid flows induced by steady solute gradients. The measured velocity profiles agree quantitatively with those predicted by analytical approximations of relevant hydrodynamic models. We discuss how the speed of gradient-driven flows depends on system parameters such as the gradient magnitude, the fluid viscosity, the channel dimensions, and the solute type. These results are useful in identifying and mitigating undesired flows within microfluidic gradient systems.

Introduction

Spatial gradients in the concentration of chemical species drive the migration of colloidal particles, lipid vesicles, and motile cells through the respective processes of diffusiophoresis, osmophoresis, and chemotaxis. In diffusiophoresis,[1,2] attractive (repulsive) interactions between solute molecules and the surface of a colloidal particle drive its motion up (down) concentration gradients, thereby increasing the number of favorable interactions. In osmophoresis,[3,4] gradients in the osmotic pressure difference across the semipermeable membrane of a lipid vesicle result in fluid flows and directed motion to regions of lower concentration. In chemotaxis,[5] motile cells such as the bacteria *E. coli* bias their stochastic run-and-tumble motion in response to chemical stimuli to swim up or down chemoeffector gradients. In addition to bacteria, the directed migration of eukaryotes in chemical gradients is critical to cancer metastasis,[6] immune response,[7] and morphogenesis.[8] These different types of gradient driven transport are often slow (of order 1 μm s^{-1}) and compete with those due to Brownian motion and fluid convection to direct the movement of biological and non-biological colloids alike. The quantitative study of these phenomena requires well-characterized experimental platforms, in which to create solute gradients, control fluid flow, and capture colloidal motions.

In this context, microfluidic systems offer a variety of strategies for creating transient or steady solute gradients with or without external flows.[9–12] Chemical gradients are readily achieved using diffusive transport along channels connecting two reservoirs that contain solutions of different concentrations—a high concentration "source" and a low concentration "sink". In the simplest case, exemplified by traditional Zigmond[13] and Dunn[14] chambers used in chemotaxis assays, the reservoirs are closed, and the concentration gradient decays in time as the system equilibrates. Steady gradients are created using fluid flow to maintain the concentrations within the respective reservoirs. Often, however, such flows lead to fluid motion in the channel connecting the reservoirs, potentially disrupting the solute gradient and/or gradient driven motions therein. To address this challenge, microfluidic systems have been developed using hydrogel membranes to separate the flowing reservoir streams from the quiescent gradient region. Wu *et al.* fabricated a microfluidic system from an agarose hydrogel that permits the diffusive exchange of solutes between neighboring channels;[15] Squires *et al.* used projection lithography to photopolymerize thin hydrogel membranes between the channels of standard PDMS-based devices;[16] Luo *et al.* used the rapid complexation of oppositely charged polyelectrolytes to create biopolymer membranes at the interface between two co-flowing streams.[17,18] Owing to their small size and continuous reservoir streams, these systems allow for the rapid generation and indefinite maintenance of steady solute gradients isolated from external flows.

Department of Chemical Engineering, Columbia University, New York, NY, USA.
E-mail: kyle.bishop@columbia.edu

† Electronic supplementary information (ESI) available: Details of the data analysis and results of the hydrodynamic model. See DOI: 10.1039/c8lc00526e

However, even in the absence of external flows, concentration gradients can themselves induce steady convection due to buoyancy[19] and to diffusioosmosis.[2] Buoyancy driven flows arise when gravity acts perpendicular to the concentration gradient due to spatial variations in the fluid density. Diffusioosmotic flows arise due to interactions between the solute and the channel walls, resulting in finite slip velocities directed parallel to the solute gradient. In microfluidic systems, the flow velocities due to solute gradients can vary from 0.1 to 10 μm s^{-1} depending on properties such as the channel dimensions, fluid viscosity, solute type, and gradient magnitude among others. The presence and potential impact of such flows are often overlooked, even when the phenomena of interest involve motions at similar speeds. The chemotactic velocity of motile bacteria is typically 0.1–1 μm s^{-1};[20] the diffusiophoretic velocities of micron-scale colloids fall within a similar range.[2] Our interest in gradient-driven fluid flows grew from a desire to quantify the similarly slow motions of lipid vesicles in solute gradients *via* osmophoresis.[3,4] A quantitative understanding of these flows is required to account or mitigate for their potentially disruptive impacts on the study of colloidal motions. At the same time, such flows can also prove useful as illustrated by demonstrations of buoyancy-driven transport *via* enzyme micropumps[21,22] and diffusioosmotic transport into dead-end pores.[23]

Here, we investigate the convective flows that accompany the formation of steady solute gradients within a microfluidic gradient generator. Building on previous designs, we use the *in situ* formation of biopolymer membranes within a three channel device to separate the gradient region from two reservoir streams containing solutes at different concentrations (Fig. 1a and b). The resulting concentration gradients induce fluid flows due to a combination of gravitational body forces and diffusioosmotic surface forces. The velocity profiles within the gradient channel are quantified using fluorescent tracer particles as a function of system parameters such as the solute type, gradient magnitude, solution viscosity, and channel height. Our experimental observations are described quantitatively by hydrodynamic models that account for forces due to viscosity and buoyancy as well as gradient-driven flows at the channel walls. Guided by these results, we discuss how convective flows can be mitigated to enable the study of other gradient driven motions in the absence of fluid convection. Our methods and conclusions should be useful to researchers interested in quantifying cell chemotaxis as well as phoretic motions within colloidal systems.

Experiment

3-Channel microfluidic device

A 3-channel microfluidic device was fabricated in polydimethylsiloxane (PDMS) using standard methods of soft lithography (Fig. 1a).[24] In the imaging area, the three parallel channels were separated by linear arrays of circular pillars (90 μm diameter separated by δ = 80 μm gaps), designed to support the *in situ* formation of two polymer membranes sep-
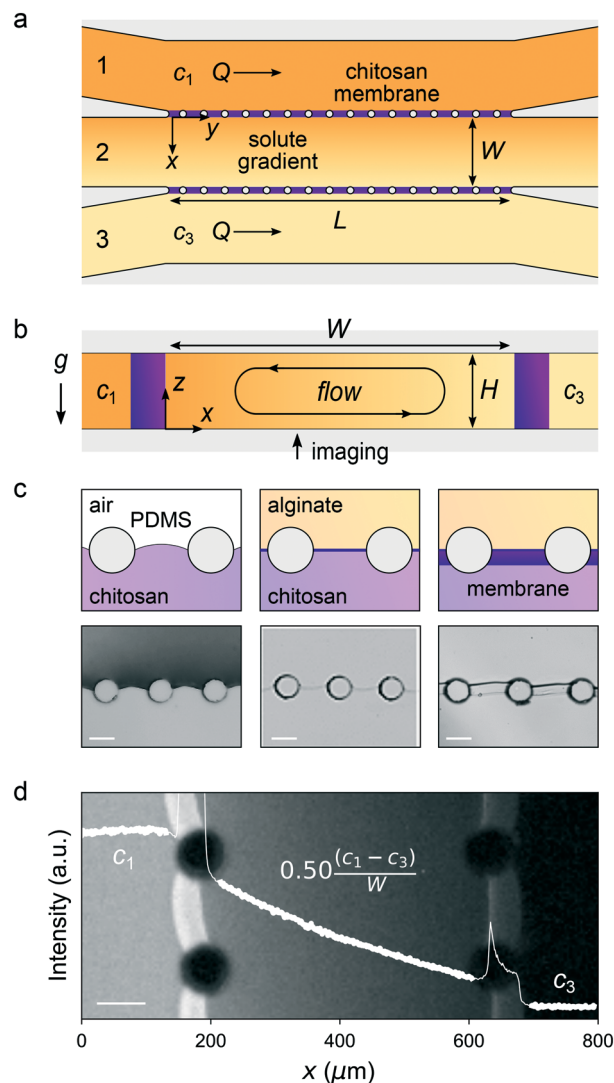

Fig. 1 (a) Schematic illustration of the three-channel microfluidic system as viewed from the top (*xy* plane). (b) Illustration of solute-driven flows as viewed down the length of the center channel (*xz* plane). (c) Three stages of the *in situ* formation of chitosan membranes. (d) Fluorescence image of the steady concentration gradient formed across the center channel; a plot of the fluorescence intensity as a function of *x* is superimposed on the image. Scale bars are 100 μm.

arating the channels (see below). The width of the central channel was 400 μm; its height was varied from H = 35 to 120 μm. The region of contact between the three channels extended over a longer length L = 2 mm, as to create uniform solute gradients spanning the central channel. Prior to use, the device was heated at 180 °C for two hours to render the PDMS surface hydrophobic with a measured water contact angle greater than 90°.

In situ membrane formation

The three channels were separated by chitosan membranes that served to prevent convective flows between the channels but allowed for the diffusive exchange of dissolved species.

These attributes allowed us to generate and maintain uniform concentration gradients indefinitely by continuous flow of solute solutions through the side channels. The membranes were fabricated using a recently reported protocol with a simplifying modification.[18]

First, an acidic chitosan solution (0.5% w/v with pH = 5.7 by addition of HCl) was flowed into the two side channels using a pressure pump. Importantly, the inlet pressure was chosen as to avoid flooding the central channel (1–3 kPa depending on channel height H). The capillary pressure required to force the meniscus through the rectangular gap between two pillars can be approximated as $\Delta p \sim \gamma(H^{-1} + \delta^{-1})$, where γ is the surface tension of the chitosan solution. Because the gap between the pillars was smaller than the channel width ($\delta < W$), the meniscus could be advanced down the channel at pressures below this critical value. After filling the side channels, the inlet pressure was increased slowly by *ca.* 50% to create convex menisci in the gaps between the pillars, as monitored by optical microscopy (Fig. 1c, left).

Next a basic solution of alginate (0.5% w/v with pH = 10 by addition of NaOH) was flowed into the center channel by a second pump at inlet pressures exceeding those applied to the side channels (3–5 kPa). At the interface between the two solutions, the oppositely charged polyelectrolytes came together to form a thin chitosan-alginate membrane (Fig. 1c, middle). This fragile membrane was reinforced by the subsequent deposition of chitosan, which precipitated onto the surface as hydroxide ions diffused into the side channels and increased the pH therein (Fig. 1c, right). The chitosan membrane grew to a desired thickness of *ca.* 30 μm over the course of five minutes, after which the channels were flushed with phosphate buffer (pH = 7.4) to terminate growth.

In contrast with the previous protocol,[18] our modification avoided the trapping of air bubbles in the gaps between neighboring pillars. Such bubbles can interfere with or prohibit the diffusive exchange of solutes between the channels and must therefore be removed or avoided. It is possible to remove trapped air bubbles *via* pressure-driven transport through PDMS into an evacuated chamber;[18] however, it's simpler to avoid them all together. By using small circular pillars and pressure driven flows, we found that careful positioning of the initial chitosan meniscus enabled the introduction of the alginate solution without trapping air.

Generation of steady concentration gradients

Steady solute gradients were established by flowing solutions of different concentrations—denoted c_1 and c_3—into the respective side channels 1 and 3 using a syringe pump. A relatively high flow rate of $Q = 0.1$ mL h^{-1} was used to ensure a nearly uniform concentration down the length of the side channels. Under these conditions, the net flux of solute through the membrane (roughly, $DcLH/W$, where D is the solute diffusivity) was much smaller than that *via* convection down the channel (cQ)—that is, $DLH/WQ \sim 0.02 \ll 1$. Owing to the small scales of the channels, a stable concentration gradient was established relatively quickly on a time scale of $W^2/D \sim 3$ min.

To visualize the solute gradient and to confirm the absence of convective flows in the central channel, we introduced a fluorescent dye (0.08 mM of calcein) to the flowing stream in channel 1. After 10 minutes, the stable concentration gradient was imaged using an inverted fluorescence microscope. The fluorescence intensity decreased linearly across the central channel as expected for steady-state diffusion between a plane source and sink (Fig. 1d). The measured gradient was 50% smaller than $(c_1 - c_3)/W$ due to additional resistances introduced by the chitosan membranes (see below).

Quantifying convective flows

Convective flows induced by the concentration gradients were quantified by particle image velocimetry (PIV) using fluorescent polystyrene (PS) tracer particles (500 nm in diameter; carboxylate-modified) dispersed in the central channel. The size of the tracers was chosen so as to limit both sedimentation (favoring smaller particles) and Brownian motion (favoring larger particles). Particles located at a prescribed height above the channel floor were imaged at regular time intervals by an inverted fluorescence microscope (10× magnification, 0.3 numerical aperture). Such images captured particles within a depth of field of *ca.* 10 μm. The resulting particle trajectories were reconstructed from the image sequences using standard particle tracking algorithms (Trackpy v0.3.2; Fig. 2a).

The tracking data was analyzed to estimate the local fluid velocity U in the imaging plane along the gradient direction (x-direction) for different heights z within the channel (Fig. 2b). The particle displacements Δ during each time interval τ were assumed to be uncorrelated and normally distributed with mean $\mu_\Delta = U\tau$ and standard deviation $\sigma_\Delta = \sqrt{2D_p\tau}$ where D_p is the particle diffusivity. As detailed in the ESI,† our analysis also accounted for spatial variations in the fluid velocity within the finite thickness of the imaging region. For simplicity, we approximated such variations by a normal distribution with mean μ_U and standard deviation σ_U. With this model, we computed the maximum likelihood estimates[25] for the unknown parameters, μ_U, σ_U, and D_p, along with their respective uncertainties using data from at least 20 particles tracked for at least 40 time intervals of 0.2 s.

Fig. 2b shows the measured velocity profile due to an applied glucose gradient. For each height z, the markers denote the average velocity within the imaging region μ_U; the error bars denote the standard deviation of the velocity in that region σ_U. Control experiments confirmed that there was no flow in the central channel in the absence of solute gradients (*i.e.*, when $c_1 = c_3$). These experiments suggest that any pressure driven flows through the chitosan membranes were negligible under the experimental conditions.
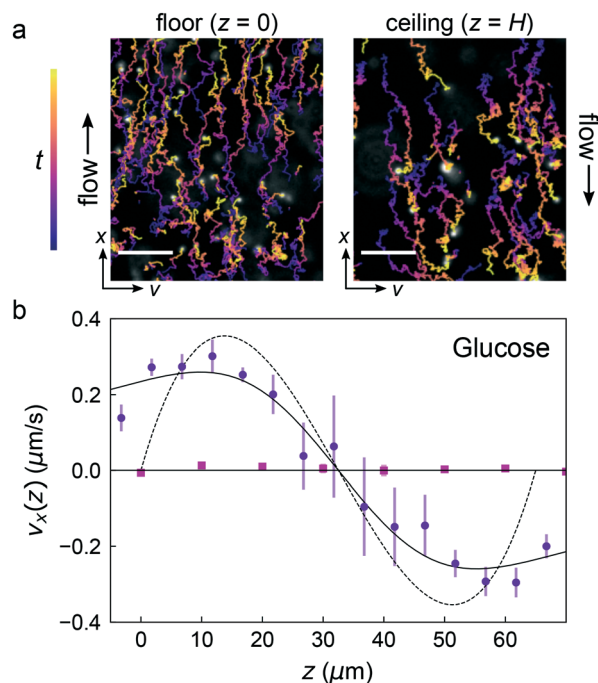
a

floor ($z = 0$)   ceiling ($z = H$)

b

Fig. 2 Glucose gradients (c_1 = 540 mM, c_3 = 40 mM) induce steady fluid flows in a channel of height H = 65 μm. (a) Visualization of the flows *via* movement of tracer particles at different heights z within the channel. Scale bars are 10 μm. (b) Steady-state velocity profile as a function of height z of the focal plane. The circular markers are experimental measurements of the mean particle velocity; error bars denote the standard deviation in the particle velocity within the imaging region. The solid curve is the theoretical prediction for the mean particle velocity; the dashed curve shows the inferred fluid velocity in the channel. The inferred magnitude of the buoyancy-driven flows is U_B = 0.46 ± 0.04 μm s^{-1}. The square markers show the mean particle velocity in the absence of the solute gradient (*i.e.*, when $c_1 = c_3$).

Hydrodynamic model

The interpretation of the experimental velocity measurements is guided by models of solute transport and fluid flow within the center channel.

Solute transport

The concentration $c(x,t)$ of the dilute solute evolves in time due to fluid convection with velocity $v(x,t)$ and to Fickian diffusion with diffusivity D,

$$\frac{\partial c}{\partial t} + v \cdot \nabla v = D\nabla^2 c. \tag{1}$$

Here, the rate of convective transport with characteristic velocity U is much slower than that of diffusive transport—that is, the Péclet number is small, Pe = $UH/D \ll 1$. In this limit, we can neglect the influence of fluid flow on the solute concentration. Moreover, we neglect variations in the concentration in both the y and z directions. Owing to the length of the channel ($L \gg W > H$), concentration variations in the y direction are expected only near its ends. There is no flux of solute through the floor or ceiling of the channel ($z = 0$ and z

= H) and therefore no concentration gradients in the z direction. At the membrane surface, we introduce a constant mass transfer coefficient k and balance the solute flux across the membrane with that into the central channel,

$$-D\frac{dc}{dx} = k(c_1 - c) \quad \text{for } x = 0. \tag{2}$$

An analogous condition applies at $x = W$. Physically, the mass transfer coefficient is related to the relative solubility of the solute in the membrane $K = c_m/c$, the solute diffusivity D_m, and the membrane thickness W_m as $k = KD_m/W_m$.

With these simplifying assumptions, the steady-state solute concentration varies linearly across the channel as

$$\frac{c_1 - c(x)}{c_1 - c_3} = \left(\frac{1}{2 + \text{Bi}}\right) + \left(\frac{\text{Bi}}{2 + \text{Bi}}\right)\frac{x}{W}, \tag{3}$$

where Bi = kW/D is a dimensionless Biot number characterizing the resistance to mass transfer through the channel relative to that through the membrane. This uniform gradient G = $-dc/dx$ develops over a characteristic time scale of order W^2/D. From the fluorescence data shown in Fig. 1d, we infer that the Biot number in our experiments is approximately Bi = 2 such that $G = 0.5(c_1 - c_2)/W$. We use the same value for other solutes, which could not be imaged directly; however, differences in solute diffusivity and solubility in the membrane can impact the resulting gradient.

Buoyancy-driven flows

The spatial variations in the solute concentration lead to similar variations in the density, which can be approximated by the linear relation $\rho/\rho_0 = 1 + \beta(c - c_0)$, where β is the solutal expansion coefficient evaluated at some reference concentration c_0. Assuming the density variations are small, the fluid velocity and pressure are well described by the so-called Boussinesq approximation,[26]

$$\nabla \cdot v = 0, \tag{4}$$

$$\rho_0\left(\frac{\partial v}{\partial t} + v \cdot \nabla v\right) = -\nabla p + \eta\nabla^2 v + \rho_0 g\beta(c - c_0). \tag{5}$$

Here, the gravitational vector is oriented in the negative z-direction $g = -ge_z$. In microfluidic systems, buoyancy driven flows are sufficiently slow that inertial effects can be safely neglected—that is, the Reynolds number is small, Re $\equiv \rho_0UH/\eta \ll 1$. In this limit, the left-hand-side of the momentum eqn (5) can be set to zero. The no slip condition implies that the fluid velocity is zero at the boundaries of the channel ($x = 0$, W and $z = 0$, H). With these simplifications, the fluid velocity and pressure distributions can be solved numerically as illustrated in Fig. 3a.†

When the height of the channel is much smaller than the width ($H \ll W$), the above equations have a simple analytical
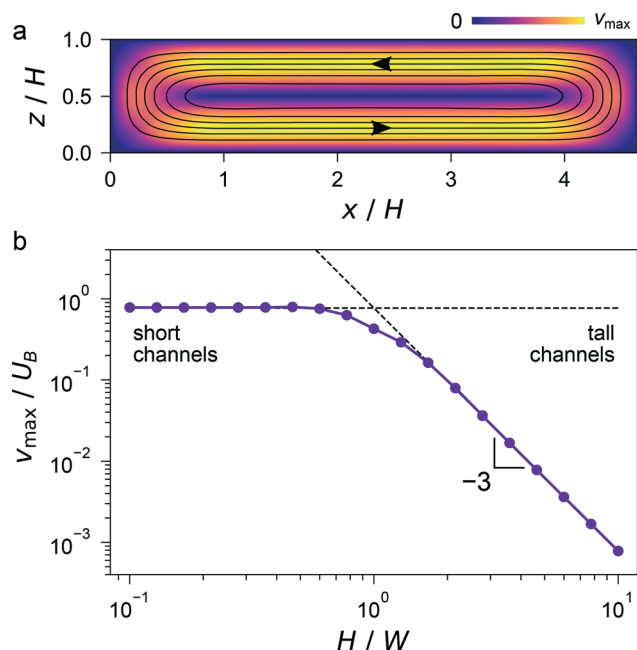
Fig. 3 (a) Computed buoyancy driven flows for a channel with aspect ratio $H/W = 0.215$. Black curves show the steamlines; the colormap shows the magnitude of the fluid velocity v. (b) Maximum fluid velocity scaled by $U_B = \beta g G H^3/96\nu$ as a function of the channel aspect ratio. The markers show the result of numerical solutions; the dashed lines show the analytical predictions for the limiting scenarios of short and tall channels. For $H \ll W$, the exact solution is well approximated by eqn (6).

solution corresponding to unidirectional flow along the x-direction.† The steady-state velocity $v_x(z)$ is given by

$$v_x(z) = U_B\left[16\left(\frac{z}{H}\right)^3 - 24\left(\frac{z}{H}\right)^2 + 8\left(\frac{z}{H}\right)\right], \quad (6)$$

where $U_B = \beta g G H^3/96\nu$ is a characteristic velocity of the flow (similar to the peak velocity, $v_{max} = 0.77U_B$). When the solute concentration increases from $x = 0$ to W ($G > 0$) and β is positive, fluid flows in the positive x-direction along the bottom half of the channel and the reverse direction along the top half (Fig. 3a). An analogous expression can be derived in the opposite limit of tall channels ($H \gg W$).† Fig. 3b shows the peak velocity for buoyancy driven flow as a function of the channel aspect ratio, highlighting the limiting behaviors for short and tall channels.

Using the above solution, we can identify the conditions under which the simplifying assumptions of small Péclet and Reynolds numbers are valid. In particular, the condition of small Péclet number implies that the height of the channel be sufficiently small that $H \ll (96D\nu/\beta g G)^{1/4}$. For a glucose concentration gradient of 100 mM mm^{-1} in water at 25 °C, the channel height must be smaller than 200 μm (for $D = 0.67 \times 10^{-9}$ m^2 s^{-1}, $\nu = 8.9 \times 10^{-7}$ m^2 s^{-1}, $\beta = 6.8 \times 10^{-5}$ m^3 mol^{-1}). For taller channels with Pe ≥ 1, buoyancy driven flows act to weaken the solute gradient thereby reducing the

flow velocity relative to the zero Péclet prediction. The condition of small Reynolds numbers is less stringent and remains valid for even larger channel heights.

Diffusioosmotic flows

In addition to buoyancy-driven convection, concentration gradients within the channel may also lead to diffusioosmosis, which results in a finite slip velocity at the surface of the channel walls. For dilute solutions of non-electrolytes,[27,28] the slip velocity at the surface of the channel wall ($z = 0$) is given by

$$U_D = -\frac{k_B T \alpha}{\eta}\frac{dc}{dx} \quad \text{(non-electrolyte)} \quad (7)$$

where $k_B T$ is the thermal energy. The parameter α is determined by the potential of mean force $\Phi(z)$, which characterizes the interaction between the solute and the surface,

$$\alpha = \int_0^\infty z[\exp(-\Phi(z)/k_B T) - 1]dz. \quad (8)$$

For the idealized case of a spherical solute of radius a that interacts with the surface only through excluded volume interactions, the above expression implies that $\alpha = -a^2/2$; fluid flows from regions of lower to higher solute concentration. Approximating glucose as a non-interacting solute with $a = 0.4$ nm, a gradient of 100 mM mm^{-1} in water is predicted to drive fluid flows at speeds of only 10 nm s^{-1}. By contrast, solutes that interact favorably with the surface can result in slip velocities that are orders-of-magnitude larger and directed from high to low solute concentrations.[2]

While diffusioosmosis can often be neglected for uncharged solutes, concentration gradients in dilute electrolytes can generate slip velocities as large as 10 μm s^{-1} along charged surfaces.[23] For symmetric z:z electrolytes,[28,29] the slip velocity is given by

$$U_D = -\frac{3D_B}{2z^2}\left[\beta\tilde{\zeta} + 4\ln\cosh\frac{\tilde{\zeta}}{4}\right]\frac{1}{c}\frac{dc}{dx} \quad \text{(electrolyte)}, \quad (9)$$

where $\tilde{\zeta} = e\zeta/k_B T$ is the zeta potential of the surface scaled by the thermal potential, $D_B = k_B T/6\pi\eta\lambda_B$ is a characteristic diffusivity based on the Bjerrum length $\lambda_B = e^2/4\pi\varepsilon k_B T$, and $\beta = (D_+ - D_-)/(D_+ + D_-)$ describes the diffusivity difference between cation and anion.[2] For water at 25 °C, the Bjerrum length is $\lambda_B = 0.7$ nm, corresponding to $D_B = 3 \times 10^{-10}$ m^2 s^{-1}. The quantities in brackets are typically of order unity—for example, $\beta = -0.21$ for NaCl (ref. 30) and $\tilde{\zeta} = -1$ for PDMS at pH = 7 in 10 mM NaCl.[31]

Importantly, diffusioosmosis driven by electrolyte gradients depends on both the concentration gradient and the local concentration. For the homogeneous gradients studied here, the largest slip velocities are expected to occur on the low concentration side of the channel. Owing to the significant membrane resistance (Bi = 2), the maximum possible

gradient in our system is limited to $d \ln c / dx = 2/W$, which corresponds to a slip velocity of 0.7 $\mu m\ s^{-1}$ using the above estimates for the relevant parameters. Such velocities are comparable to those of buoyancy-driven flows and are therefore considered in our analysis of ionic solutes.

For short channels ($H \ll W$), the lubrication approximation can be used to derive the following velocity profile within the central channel,†

$$v_x(x,z) = U_D(x)\left[6\left(\frac{z}{H}\right)^2 - 6\left(\frac{z}{H}\right) + 1\right], \quad (10)$$

where $U_D(x)$ is the diffusioosmotic slip velocity, which varies with position across the channel. Owing to the linearity of the equations governing low Reynolds number flow, such diffusioosmotic flows can be superimposed onto the buoyancy-driven flows detailed in the previous section.

Finally, in addition to the diffusioosmosis at the floor and ceiling of the channel, similar flows arise at the surface of the tracer particles resulting in their motion parallel to the concentration gradient. The diffusiophoretic velocity of the particles is equal and opposite to the slip velocity presented in eqn (9). Such motions contribute a spatially uniform shift in the measured tracer particle velocity and must be considered when measuring fluid flows driven by electrolyte gradients (see below).

Results and discussion

We first consider flows driven by glucose gradients, for which buoyancy is the dominant driving force and diffusioosmosis can be neglected. For a channel of height $H = 65\ \mu m$, an imposed concentration difference of 500 mM resulted in buoyancy-driven flows with a characteristic magnitude of $U_B = 0.46 \pm 0.04\ \mu m\ s^{-1}$ as inferred from the data in Fig. 2b. The parameter estimates and the fitted velocity profile (solid curve) were obtained using Bayesian inference[25] with Markov chain Monte Carlo (MCMC) sampling and the hydrodynamic model outlined above.† The measured velocity profile as a function of height z agrees with the predictions of eqn (6), when accounting for the finite thickness of the imaging region. For the experimental conditions, the model predicts that $U_B = 1.0\ \mu m\ s^{-1}$, roughly twice that observed in experiment. One possible explanation for the discrepancy is that the chitosan membranes are less permeable to glucose than to the fluorescent dye used to estimate the membrane resistance. Previous studies support this possibility by showing that chitosan membranes are *ca.* four times more permeable to NaCl than to glucose.[32,33] A comparable four-fold reduction in the Biot number from Bi = 2 to 0.6 is necessary to reconcile the discrepancy between experiment and theory.

Perhaps more important than the precise magnitude of buoyancy-driven flows is their scaling dependence on various system parameters such as the concentration difference $\Delta c = c_1 - c_3$, the viscosity η, and the channel height H. Fig. 4a
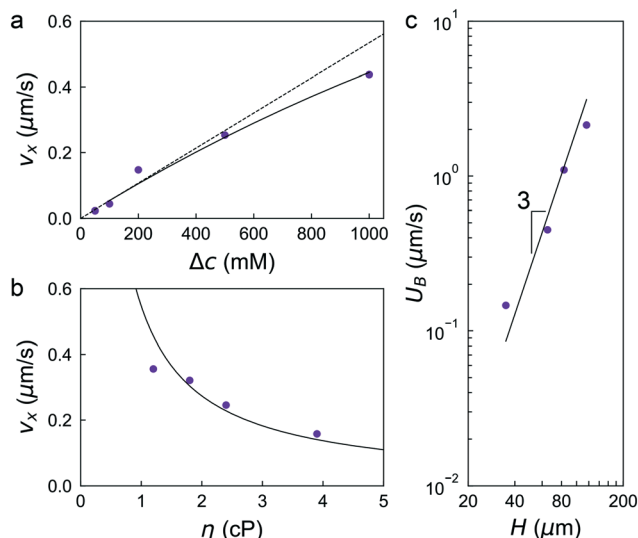

Fig. 4 Buoyancy-driven flows due to glucose gradients depend on the concentration difference $\Delta c = c_3 - c_1$, the solution viscosity η, and the channel height H. (a) The measured velocity increased linearly with the concentration difference. Other parameters were held constant: $W = 400\ \mu m$, $H = 65\ \mu m$. The solid curve shows predicted deviations from the linear trend due to changes in the solution viscosity with increasing glucose concentration. (b) The measured velocity decreased with increasing viscosity due to addition of PEG600. Other parameters were held constant: $W = 400\ \mu m$, $H = 65\ \mu m$, $c_1 = 540$ mM, $c_3 = 40$ mM. (c) The inferred magnitude of buoyancy drive flows U_B increased with channel height H as $U_B \propto H^3$. Other parameters were held constant: $W = 400\ \mu m$, $c_1 = 540$ mM, $c_3 = 40$ mM.

shows how the measured flow velocity increases linearly with the difference in solute concentrations applied across the channel. These experiments were performed using the same gradient generator ($H = 65\ \mu m$) and the same focal region ($z \sim 5\ \mu m$). The glucose concentration in channel 1 was increased from $c_1 = 90$ mM to 1040 mM; the concentration in channel 3 was held constant at $c_3 = 40$ mM. Following each change in the concentration, the system was allowed to relax to the new steady-state (at least 10 min) before data collection. At high concentrations, the expected linear dependence on concentration is also influenced by the concomitant increase in the solution viscosity: the kinematic viscosity of 1 M glucose is 60% higher than pure water at $T = 20$ °C. The solid curve in Fig. 4a shows the model prediction accounting for the increase in solution viscosity.

One strategy for mitigating buoyancy-driven flows is to increase the viscosity of the solution. To demonstrate this effect, we flowed aqueous solutions of PEG600 in different concentrations into the central channel to alter the viscosity therein. As predicted, the measured flow velocity due to an applied glucose gradient ($c_1 = 540$ mM, $c_3 = 40$ mM) decreased inversely with increasing viscosity (Fig. 4b). The addition of 250 g L^{-1} of PEG600 induced a four-fold increase in the viscosity and a comparable decrease in the speed of buoyancy-driven flows. This approach is particular useful for studies of osmophoresis, which does not depend on the viscosity of the surrounding fluid.[3]

The most effective strategy for mitigating buoyancy-driven flows is to reduce the height of the channel, thereby increasing the viscous resistance to fluid motion and decreasing the gravitational pressure difference (Fig. 4c). The characteristic velocity scale U_B is predicted to increase as the cube of the channel height H. To demonstrate this dependence, we prepared a series of devices with channel heights ranging from $H = 35$ μm to 120 μm. For each device, we applied a glucose concentration difference of 500 mM across a width of $W = 400$ μm and measured the velocities of tracer particles at different heights within the channel. From these data, we inferred the velocity magnitude U_B for each device as described above and in Fig. 2. The velocity increased by more than an order of magnitude as the channel height was increased by a factor of three (Fig. 4c) in reasonable agreement with the theoretical prediction.

Electrolyte gradients

In addition to buoyancy driven flows, electrolyte gradients are accompanied by diffusiomotic flows in the channel as well as diffusioosmotic motions of the tracer particles. Fig. 5 shows the measured velocity profile within a channel of height $H = 65$ μm due to a NaCl gradient with reservoir concentrations $c_1 = 677$ mM and $c_3 = 177$ mM. In analyzing these data,† we considered three independent contributions: buoyancy driven flows as described by eqn (6), diffusioosmotic flows as described by eqn (9), and diffusiophoretic motions of the tracer particles. The magnitude of the buoyancy driven flows was inferred to be $U_B = 1.1 \pm 0.05$ μm s^{-1}, as compared to the theoretical prediction of $U_B = 0.7$ μm s^{-1} for Bi = 2. Again, these differences can be resolved by accounting for possible differences in the membrane resistance for the different solutes; for NaCl, a physically reasonable Biot number

of Bi = 6 resolves the discrepancy between experiment and theory.

The speed of particle diffusiophoresis averaged across the channel width was inferred to be $U_{DP} = -0.20 \pm 0.03$ μm s^{-1}, with particles moving towards regions of high salt concentrations. This behavior is consistent with the predictions of eqn (9) when accounting for the measured zeta potential of the polystyrene tracer particles $\zeta = -29$ mV in 500 mM NaCl. For the experimental conditions and assuming Bi = 6, eqn (9) predicts an average diffusiophoretic velocity of $U_{DP} = -0.28$ μm s^{-1}. Similarly, the magnitude of the diffusioosmotic flows averaged across the channel width was inferred to be $U_{DO} = 0.2 \pm 0.1$ μm s^{-1}, as compared to $U_{DO} = 0.23$ μm s^{-1} predicted by theory assuming $\zeta = -25$ mM for the PDMS walls.[31]

Here, diffusioosmotic flows are smaller than those due to buoyancy; however, that need not be the case. For small membrane resistances (Bi ≫ 1) and low sink concentrations ($c_3 \to 0$), the diffusiosmotic velocity near the sink ($x = W$) scales as $U_D \sim 3BiD_B/2W$, which can exceed 10 μm s^{-1} for highly permeable membranes Bi > 10 and/or narrow channels $W < 400$ μm. In contrast to buoyancy driven flows, diffusiophoretic flows do not depend on the channel height H nor the absolute magnitude of the concentration difference Δc. Consequently, such flows may be present even in short channels due to small concentration differences, provided these differences are comparable to the concentrations themselves—that is, $\Delta c \sim c$. The most effective strategy for mitigating such flows is to use concentration gradients in which the minimum concentration is comparable in magnitude to the maximum concentration—that is, $c_3 \sim c_1$ such that $\Delta c \ll c$.

Temperature dependence

The above experiments were conducted at room temperature (22 °C); however, the magnitude of gradient driven flows are expected to vary with temperature. Such variations may be important to consider in studies of chemotaxis and cell migration at physiological temperatures (37 °C). For buoyancy driven flows, the temperature influences both the solutal expansion coefficient β and the kinematic viscosity v. For example, the kinematic viscosity of glucose in water (500 mM) decreases with increasing temperature at a rate of ca. 2% per °C.[34] Similarly, the solutal expansion coefficient of glucose in water decreases at a rate of ca. 0.5% per °C.[34] One would therefore expect that buoyancy driven flows would be ca. 30% larger at physiological temperatures.

Conclusions

In sum, solute gradients drive steady flows at speeds of several microns per second even within the small channels of microfluidic systems. These flows arise due to a combination of gravitational body forces and diffusiophoretic surface forces and are well described by simple hydrodynamic models. Such models predict how gradient driven flows depend on relevant system parameters such as the gradient magnitude, solution viscosity, channel dimensions, and
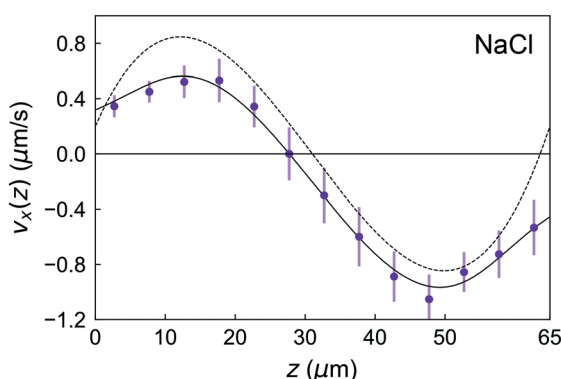

Fig. 5 Steady-state velocity profile as a function of height z of the focal plane for an NaCl gradient ($c_1 = 677$ mM, $c_3 = 177$ mM) in a channel of height $H = 65$ μm. The markers are experimental measurements of the mean particle velocity; error bars denote the standard deviation in the particle velocity within the imaging region. The solid curve is the theoretical prediction for the mean particle velocity; the dashed curve shows the inferred fluid velocity in the channel. The inferred velocities are $U_B = 1.1 \pm 0.05$ m s^{-1} for buoyancy-drive flow, $U_{DO} = 0.2 \pm 0.1$ μm s^{-1} for diffusioosmotic flow, and $U_{DP} = -0.2 \pm 0.03$ μm s^{-1} for diffusiophoretic particle motions.

solute type. These predictions are useful in guiding the design of microfluidic gradient generators, in which fluid flows are effectively eliminated. The mitigation of gradient driven flows is relevant to the study of other types of colloidal motion in solute gradients—most notably, particle diffusiophoresis, vesicle osmophoresis, and cell chemotaxis. In particular, failure to account for such flows can lead to significant errors in quantifying the chemotaxis of bacteria populations (Fig. S1†).

Conflicts of interest

There are no conflicts to declare.

Acknowledgements

References

1 J. L. Anderson, M. E. Lowell and D. C. Prieve, *J. Fluid Mech.*, 1982, **117**, 107–121.
2 J. S. Paustian, C. D. Angulo, R. Nery-Azevedo, N. Shi, A. I. Abdel-Fattah and T. M. Squires, *Langmuir*, 2015, **31**, 4402–4410.
3 J. L. Anderson, *Phys. Fluids*, 1983, **26**, 2871–2879.
4 J. Nardi, R. Bruinsma and E. Sackmann, *Phys. Rev. Lett.*, 1999, **82**, 5168–5171.
5 H. Mao, P. S. Cremer and M. D. Manson, *Proc. Natl. Acad. Sci. U. S. A.*, 2003, **100**, 5449–5454.
6 E. T. Roussos, J. S. Condeelis and A. Patsialou, *Nat. Rev. Cancer*, 2011, **11**, 573–587.
7 P. N. Devreotes and S. H. Zigmond, *Annu. Rev. Cell Biol.*, 1988, **4**, 649–686.
8 D. Ambrosi, A. Gamba and G. Serini, *Bull. Math. Biol.*, 2004, **66**, 1851–1873.
9 T. M. Keenan and A. Folch, *Lab Chip*, 2008, **8**, 34–57.
10 S. Kim, H. J. Kim and N. L. Jeon, *Integr. Biol.*, 2010, **2**, 584–603.
11 J. Wu, X. Wu and F. Lin, *Lab Chip*, 2013, **13**, 2484–2499.
12 E. Berthier and D. J. Beebe, *Lab Chip*, 2014, **14**, 3241–3247.
13 S. H. Zigmond, *J. Cell Biol.*, 1977, **75**, 606–616.
14 D. Zicha, G. A. Dunn and A. F. Brown, *J. Cell Sci.*, 1991, **99**, 769–775.
15 S.-Y. Cheng, S. Heilman, M. Wasserman, S. Archer, M. L. Shuler and M. Wu, *Lab Chip*, 2007, **7**, 763–769.
16 J. S. Paustian, R. N. Azevedo, S. T. B. Lundin, M. J. Gilkey and T. M. Squires, *Phys. Rev. X*, 2014, **3**, 041010.
17 X. Luo, T. Vo, F. Jambi, P. Pham and J. S. Choy, *Lab Chip*, 2016, **16**, 3815–3823.
18 P. Pham, T. Vo and X. Luo, *Lab Chip*, 2017, **17**, 248–255.
19 T. M. Squires and S. R. Quake, *Rev. Mod. Phys.*, 2005, **77**, 977–1026.
20 K. Son, F. Menolascina and R. Stocker, *Proc. Natl. Acad. Sci. U. S. A.*, 2016, **113**, 8624–8629.
21 S. Sengupta, D. Patra, I. Ortiz-Rivera, A. Agrawal, S. Shklyaev, K. K. Dey, U. Córdova-Figueroa, T. E. Mallouk and A. Sen, *Nat. Chem.*, 2014, **6**, 415–422.
22 O. E. Shklyaev, H. Shum, A. Sen and A. C. Balazs, *Sci. Adv.*, 2016, **2**, e1501835.
23 A. Kar, T. Y. Chiang, I. Ortiz Rivera, A. Sen and D. Velegol, *ACS Nano*, 2015, **9**, 746–753.
24 Y. Xia and G. M. Whitesides, *Annu. Rev. Mater. Sci.*, 1998, **28**, 153–184.
25 D. S. Sivia and J. Skilling, *Data Analysis: A Bayesian Tutorial*, Oxford University Press, New York, 2nd edn, 2006.
26 D. D. Gray and A. Giorgini, *Int. J. Heat Mass Transfer*, 1976, **19**, 545–551.
27 J. L. Anderson, M. E. Lowell and D. C. Prieve, *J. Fluid Mech.*, 1982, **117**, 107–121.
28 J. J. Anderson, *Annu. Rev. Fluid Mech.*, 1989, **21**, 61–99.
29 J. L. Anderson, M. E. Lowell and D. C. Prieve, *J. Fluid Mech.*, 1982, **117**, 107–121.
30 D. Velegol, A. Garg, R. Guha, A. Kar and M. Kumar, *Soft Matter*, 2016, **12**, 4686–4703.
31 B. J. Kirby and E. F. Hasselbrink, *Electrophoresis*, 2004, **25**, 203–213.
32 B. Krajewska and A. Olech, *Polym. Gels Networks*, 1996, **4**, 33–43.
33 B. Krajewska, *React. Funct. Polym.*, 2001, **47**, 37–47.
34 J. F. Comesaña, J. J. Otero, E. García and A. Correa, *J. Chem. Eng. Data*, 2003, **48**, 362–366.